

Dry Deposition Methods Based on Turbulence Kinetic Energy: Part 2. Extension to Particle Deposition Using a Single-Point Model

Bin Cheng¹, Kiran Alapaty², Qian Shu¹, and Saravanan Arunachalam³

¹ORISE/US EPA

²US EPA

³University of North Carolina at Chapel Hill

November 26, 2022

Abstract

Magnitude of atmospheric turbulence, a key driver of several processes that contribute to aerosol (i.e., particle) deposition, is typically underrepresented in current models. Various formulations have been developed to model particle dry deposition; all these formulations typically rely on friction velocity and some use additional ad hoc factors to represent enhanced impacts of turbulence. However, none were formally linked with the three-dimensional (3-D) turbulence. Here, we propose a set of 3-D turbulence-dependent resistance formulations for particle dry deposition simulation and intercompare the performance of new resistance formulations with that obtained from using the existing formulations and measured dry deposition velocity. Turbulence parameters such as turbulence velocity scale, turbulence factor, intensity of turbulence, effective sedimentation velocity, and effective Stokes number are newly introduced into two different particle deposition schemes to improve turbulence representation. For an assumed particle size distribution, the newly proposed schemes predict stronger diurnal variation of particle dry deposition velocity and are comparable to corresponding measurements while existing formulations indicate large underpredictions. We also find that the incorporation of new turbulence parameters either introduced or added stronger diurnal variability to sedimentation velocity and collection efficiencies values, making the new schemes predict higher deposition values during daytime and nighttime when compared to existing schemes. The findings from this research may help improve the capability of dry deposition schemes and help fostering the community dry deposition modeling system for use in regional and global models.

Hosted file

essoar.10510622.1.docx available at <https://authorea.com/users/554731/articles/605731-dry-deposition-methods-based-on-turbulence-kinetic-energy-part-2-extension-to-particle-deposition-using-a-single-point-model>

Hosted file

si-paper-2-aerosols-for-submissionjgr_02112022.docx available at <https://authorea.com/users/554731/articles/605731-dry-deposition-methods-based-on-turbulence-kinetic-energy-part-2-extension-to-particle-deposition-using-a-single-point-model>

Bin Cheng¹, Kiran Alapaty², Qian Shu¹, and Saravanan Arunachalam³

¹Postdoctoral Research Participant, Oak Ridge Institute for Science and Education/Office of Research and Development/Center for Environmental Measurement and Modeling/Atmospheric and Environmental Systems Modeling Division /U.S. Environmental Protection Agency, Research Triangle Park, North Carolina, USA.

²Center for Environmental Measurement and Modeling, Office of Research and Development, U.S. Environmental Protection Agency, Research Triangle Park, North Carolina, USA.

³Institute for the Environment, The University of North Carolina at Chapel Hill, Chapel Hill, North Carolina, USA.

Corresponding author: Kiran Alapaty (alapaty.kiran@epa.gov)

Key Points:

- New turbulence parameters are introduced to improve particle deposition estimation
- New dry deposition formulations largely reduce biases in deposition velocity estimations

Submitted to JGR-A on February 11, 2022

(A companion manuscript with the Part-1 for gas dry deposition)

Abstract

Magnitude of atmospheric turbulence, a key driver of several processes that contribute to aerosol (i.e., particle) deposition, is typically underrepresented in current models. Various formulations have been developed to model particle dry deposition; all these formulations typically rely on friction velocity and some use additional ad hoc factors to represent enhanced impacts of turbulence. However, none were formally linked with the three-dimensional (3-D) turbulence. Here, we propose a set of 3-D turbulence-dependent resistance formulations for particle dry deposition simulation and intercompare the performance of new resistance formulations with that obtained from using the existing formulations and measured dry deposition velocity. Turbulence parameters such as turbulence velocity scale, turbulence factor, intensity of turbulence, effective sedimentation velocity, and effective Stokes number are newly introduced into two different particle deposition schemes to improve turbulence representation. For an assumed particle size distribution, the newly proposed schemes predict stronger diurnal variation of particle dry deposition velocity and are comparable to corresponding measurements while existing formulations indicate large underpredictions. We also find that the incorporation of new turbulence parameters either introduced or added stronger diurnal variability to sedimentation velocity and collection efficiencies values, making the new schemes predict higher deposition values during daytime and nighttime when compared to existing schemes.

The findings from this research may help improve the capability of dry deposition schemes and help fostering the community dry deposition modeling system for use in regional and global models.

Plain Language Summary

Aerosols, also known as particulate matter, in the atmosphere can affect ecosystem health through a process called dry deposition and is a helpful process that can reduce human exposure to air pollutants. There are several processes involved in particle dry deposition and one of the most important processes is the chaotic motions of the atmosphere, which is known as turbulence. However, turbulence strength is underrepresented in mathematical modeling of particle dry deposition. In this study, we introduced several turbulence parameters to improve the representation of turbulence effects on deposition and introduced new formulations. These new formulations are tested in a simple mathematical model and then field measurements are used to evaluate the performance of new formulations as well as existing formulations. Results indicate that the new formulations largely improved results, which are closer to measurements while existing formulations showed large underestimations. This research offers improved capability of models in estimating particle deposition and in turn hopefully leads to better estimation of particle pollution and related exposures.

1 Introduction

Atmospheric aerosols (liquid and solid), hereafter referred to as particles, have substantial influences on the air quality, radiative balance of the earth, climate, and ecosystem (e.g., Fowler et al., 2009; Lee et al., 2013). Dry deposition is the process that removes gases and aerosols from the air (e.g., Pryor et al., 2008) and is a source of many nutrients to natural ecosystems. Large uncertainties exist in the modeling of particle dry deposition leading to more uncertainties in the estimation of (1) aerosol direct, semi-direct, and indirect effects in climate models; (2) damages to environment via impairment and shifts in biodiversity and health of vegetation; (3) critical loads of nutrients affecting terrestrial ecosystem, and (4) human health impacts via exposure to pollutants. Thus, refined deposition formulations and updated comprehensive measurements are needed to improve estimation of particle dry deposition to address these important topics (Farmer et al., 2021).

Particle dry deposition is driven by atmospheric turbulence and exhibits a significant relationship with particle size distribution (PSD) as well as strong dependence on land use/land cover types (e.g., Slinn, 1982; Wesely, 1985; Riemer et al., 2019). Particle dry deposition is controlled by various processes including Brownian diffusion, gravitational settling, interception, and impaction while the contributions of these deposition processes to particle dry deposition velocities vary substantially (Zhang and Shao, 2014; Hicks et al., 2016). Saylor et al. (2019) reported that depending upon the type of dry deposition scheme used, particle dry deposition predictions for forest land may differ by over 200%. The PSD also determines the characteristics of particle deposition dynamics where

deposition of smaller particles (<300 nm) tended to be driven by Brownian diffusion, while interception, impaction, and gravitational settling have greater impacts on larger particles (Erisman and Draaijers, 1995; Emerson et al., 2020). In various models, many distinct methods were employed to represent the PSD characteristics, e.g., single particle diameter, discrete size bins, and continuous lognormal distributions (Seinfeld and Pandis, 2016; Riemer et al., 2019), and these different approaches also added some uncertainties to the estimation of particle dry deposition velocity (Shu et al., 2017). Moreover, deposition surfaces such as terrestrial and hydrological surfaces remove particles at different rates due to the various characteristics of the surfaces, and land cover with larger surface area with more collectors tended to induce greater deposition rates (e.g., forest $>$ grassland $>$ lakes) (Farmer et al., 2021).

Farmer et al. (2021) provided a comprehensive review of dry deposition of aerosols that include various approaches used, measurements available as of present, and modeling outcomes. They listed size-resolved particle flux measurements that are available to researchers for four different types of land use categories (two vegetative, water, and snow/ice) as well as instrumental methods used along with particle size range and associated deposition velocity. For grass and forests, it was shown that the average lower and upper bounds of measured dry deposition velocity can be around ~ 0.01 to ~ 10 cm s^{-1} , which is about three orders of magnitude range, depending upon the particle diameter (0.001 to 100 μm). The strong association between deposition velocity and particle diameter signifies the importance of accurately estimating particle diameter. These very limited measurements reflect the scarcity and huge data gaps for particle deposition modeling and evaluation. They also mentioned that friction velocity plays an important role in modulating particle flux while more turbulent conditions (e.g., convective conditions) induced stronger flux. While consistent meteorological and particle measurements are much needed for a long-term period to evaluate existing formulations establishing statistical significance of their accuracy, there is also a need to realistically represent turbulence effects on particle deposition in the existing formulations.

Essential resistances included in a particle dry deposition model are aerodynamic resistance and surface resistance (e.g., Saylor et al., 2019), both strongly influenced by the strength of the atmospheric turbulence and thus more turbulent conditions may lead to higher particle deposition fluxes (Sievering, 1987; Ahlm et al., 2010; Saylor et al., 2019). Recognizing the inadequacy of using friction velocity alone for representing strong turbulence effects, Wesely et al. (1985) have introduced an empirical formulation to represent the enhanced role of turbulence, thereby estimated higher deposition rates were found to be comparable to observed deposition rates. Saylor et al., (2019) showed that depending on the value of the convective velocity (w_*), estimated dry deposition can differ by as much as about a factor of 10. This result signified the uncertainty arising from using empirical formulations to enhance turbulence effects on particle deposition that were not rigorously evaluated. Many particle deposition formulations and related sub-formulations (e.g., Zhang et al., 2001) used in regional and global air

quality models are still based on solely friction velocity, offering an opportunity to improve the representation of turbulence effects in such schemes, which is the focus of this research. This paper is a companion paper to the Part-1 by Alapaty et al., (2022) that focused on gas deposition and here we adopt the major findings from that paper to improve turbulence representations for particle deposition.

None of the deposition schemes for gases and particles utilize the three-dimensional (3-D) turbulence (i.e., variances of velocity fluctuations) to represent effects of turbulence on deposition. In the companion paper (Part-1, Alapaty et al., 2022), we have developed a new velocity scale and validated it for use in dry deposition of ozone at a decadal timescale using a single-point model. This velocity scale, known as turbulence velocity scale, was derived from using the surface turbulence kinetic energy equation that includes 3-D aspects of turbulence. In this study, we extended our previous research by proposing and validating new resistance formulations for particle dry deposition by introducing the few turbulence parameters for better representation of turbulence effects.

Thus, the objectives of this research are to (1) improve the turbulence representation in particle deposition formulations and related sub-formulations, and (2) evaluate the performance of these new formulations using available measurements and a single-point model.

2 Methods, Measurements, and Model

There are several processes involved in the particle deposition modeling. Before describing particle deposition schemes used in this study, we begin with the presentation of some of the processes (methods) in which turbulence representation can be improved. First, we briefly describe the estimation of turbulence velocity while full details can be found in the Part-1 paper. Second, we show how turbulence effects in a few particle deposition processes can be improved. This way, all new developments can be easily found in this section rather than scattering them in various subsections.

2.1 Turbulence velocity scale

Almost all gas and particle deposition formulations use friction velocity (u_*) for all stability regimes in the planetary boundary layer (PBL). Since u_* is only applicable for neutral conditions, different stability correction parameters are used for each stability regimes of PBL to account for turbulence generated by buoyancy and/or shear production. Thus, a large number of different stability functions appeared in the literature suiting the needs of an atmospheric model, which led to different modeling outcomes (Liu et al., 2007; Toyota et al., 2016). To alleviate this type of issue, Alapaty et al. (2022) have proposed a new approach where resistance formulations are functions of turbulence generated by shear and buoyancy production for different PBL stability regimes. It was achieved by using surface turbulence kinetic energy (TKE) approximations so that a single velocity scale will be suitable for different stability conditions in

the PBL. In that methodology, described in our companion paper (Part-1), the mean TKE of eddies near the surface was written as (Alapaty et al., 2022):

$$TKE = \overline{e'^2} = \frac{1}{2} (\overline{u'^2} + \overline{v'^2} + \overline{w'^2}) \quad (1)$$

where e is mean velocity, u , v , and w is eastward, northward, and vertical components of wind, superscript *prime* denotes fluctuations. Then, terms on the right-hand side of the Eq. (1) were rewritten in terms of respective variance of velocity fluctuations as:

$$\overline{e'^2} = \frac{1}{2} (\sigma_u^2 + \sigma_v^2 + \sigma_w^2) \quad (2a)$$

where σ is standard deviation. Alapaty et al., (2022) defined the turbulence velocity scale (e_*) representative of turbulence created by mechanical and buoyant forces at the surface as:

$$e_* = \sqrt{\overline{e'^2}} = \sqrt{\frac{1}{2} (\sigma_u^2 + \sigma_v^2 + \sigma_w^2)} \quad (2b)$$

Following that study the new turbulence velocity scale, e_* from the above equations can be rewritten for unstable conditions (i.e., when surface sensible heat flux > 0) in the PBL as:

$$e_* = \sqrt{3.8u_*^2 + 0.22w_*^2 + 1.9u_*^2(-z/L)^{2/3}} \quad (3a)$$

where z is the measurement height and L is Monin-Obukhov length, and for stable conditions in PBL (surface sensible heat flux < 0):

$$e_* = \sqrt{3.8u_*^2} \quad (3b)$$

An advantage of the above equations is that the parameterized e_* transitions smoothly from one stability regime to another since the 2nd and 3rd terms on the right side of Eq. 3a drop out for stable conditions. For neutral conditions that exist infrequently, e_* can be made equal to u_* as a transition point. By using 3-D variances measured by the 3-D sonic anemometer for a decadal period, Alapaty et al. (2022) hypothesized and verified that 3-D sonic anemometer measurements of friction velocity (u_{*c}) (that includes contributions by vertical heat flux to the vertical transport of horizontal momentum) can be approximated as the product of the von Karman constant (k) and turbulence velocity scale, e_* , as:

$$u_{*c} = ke_* \quad (4)$$

Note that the friction velocity (u_{*c}) that is used in modeling studies is applicable only to neutral conditions and thus a particular stability function is used to represent unstable/stable conditions in the PBL. The main advantage of this new velocity scale is that it includes turbulence contribution from buoyancy production as well as shear production, making it suitable for use for stable and unstable conditions in the PBL. Thus, with the usage of turbulence velocity scale there is no need to use any explicit stability functions in representing turbulence effects. That work has opened up doors to avoid the usage of a variety of stability functions reported in the literature that led to differences in

modeling results. Our methodology based on e_* can open doors to the concept of community dry deposition model. For more details, readers are referred to the companion paper (Part-1) by Alapaty et al. (2022).

2.2 Introducing generalized Turbulence Factor (T_f)

To account for increased particle deposition under convective conditions in the PBL, Wesely et al. (1985) have suggested an empirical equation to increase the deposition velocity of sulfate particles. This empirical equation was written as:

$$W_f = 0.24 \frac{w_*^2}{u_*^2} \quad (5)$$

To the best of our knowledge, the above empirical equation was neither validated with any other measurements nor compared with other formulations, but it has been widely used in many studies (e.g., Binkowski and Shanker 1995). However, our study offers such an intercomparison and thus we propose a generalized turbulence factor, T_f , a ratio of the terms on the right-hand side of the TKE equation shown in Eq. 2. The proposed T_f can be written as:

$$T_f = \frac{(\sigma_v^2 + \sigma_w^2)}{\sigma_u^2} \quad (6)$$

Using the Eq. 2 and 3, we write:

$$\frac{1}{2}(\sigma_u^2 + \sigma_v^2) = 3.8u_*^2 + 0.22w_*^2$$

$$\text{or } (\sigma_u^2 + \sigma_v^2) = 2(3.8u_*^2 + 0.22w_*^2) = 7.6u_*^2 + 0.44w_*^2 \quad (7)$$

$$\frac{1}{2}\sigma_w^2 = 1.9 u_*^2(-z/L)^{2/3}$$

$$\text{or } \sigma_w^2 = 3.8 u_*^2(-z/L)^{2/3} \quad (8)$$

The turbulence factor equation shown above (Eq. 6) is rooted in physical realism, and it is conceptually similar to ad-hoc relation, Eq. 5, suggested by Wesely et al. (1985). They stated that convective motions in PBL have nonlinear influence on particulate sulfate deposition velocity. There seems to be a physical connection between convective velocity in the PBL and the friction velocity in the surface layer influencing particle deposition velocity. Also, Wesely et al. (1983) suggested that this connection might lead to rapid multidirectional flow around surface elements and thus a connection between buoyancy and horizontal flows. They also stated that v is more strongly correlated to enhanced particle deposition than u and accordingly we gave more weight to v coefficients. Thus, the nonlinear connection between buoyancy and mechanical forces can result in wind gusts at the surface and such conditions can be responsible for enhanced particle deposition. Also, based on the turbulence data over land and ocean, Hicks (1985) documented that contribution by mechanical and buoyant forces to the total variance came from v and w for convective boundary layers. From the literature we found that magnitude of coefficients differs from one study to the other (e.g., Wyngaard and Cote, 1974; Hicks, 1985) and thus there is no universal agreement on the magnitude of these coefficients. In this study, for the u_* coefficient, we assigned 70% weight to v and 30% to u , consistent with

above described qualitative findings of Wesely et al. (1985). Accordingly, the numerator and denominator components are devised in the proposed T_f equation containing velocity variances ratios, i.e., $(\sigma_v^2 + \sigma_w^2)/\sigma_u^2$. Thus, we propose individual variances of velocity fluctuations as:

$$\sigma_u^2 = 2.28u_*^2 \quad (9a)$$

$$\sigma_v^2 = 5.32u_*^2 + 0.44w_*^2 \quad (9b)$$

$$\sigma_w^2 = 3.8u_*^2(-z/L)^{2/3} \quad (9c)$$

Then the turbulence factor Eq. 6 can be rewritten as:

$$T_f = \frac{\sigma_v^2 + \sigma_w^2}{\sigma_u^2} = \frac{(5.32u_*^2 + 0.44w_*^2) + (3.8u_*^2(-z/L)^{2/3})}{2.28u_*^2} \quad (10)$$

Note that the above equation works for all stability regimes in the PBL while Eq. 5 was designed to work only for convective conditions. For stable conditions (and neutral conditions if they exist) T_f value reduces to 2.33. At this stage we do not have any observational evidence to support this constant value, but it is based on the variance equations that were derived from several field measurements (see references cited in Part-1).

2.3 Introducing effective sedimentation velocity (V_{ge})

One of the processes responsible for particle deposition is gravitational settling velocity and is also known as terminal velocity or popularly known as sedimentation velocity (V_g). Traditionally the V_g is estimated only for still air conditions. Thus, only two forces are acting on a particle, i.e., aerodynamic drag and gravity (Hinds, 1999). Then, for a solid spherical particle vertical drag force will be balanced by gravity force and thus there is no acceleration of the particle. However, turbulent eddies present in the PBL will be another force acting on a particle and turbulence is not commonly accounted for in the estimation of sedimentation velocity. For still air, V_g can be written as (see supplemental information Text S1 for derivation):

$$V_g = \frac{gC_p d_p^2}{18\mu} \quad (11)$$

where g is acceleration due to gravity, C is the Cunningham correction factor, ρ_p is density of particle, d_p is diameter of the particle, and μ is temperature dependent viscosity of air. Since the above equation is only good for neutral conditions, we propose to introduce the effects of turbulent flows on V_g in the boundary layer. In particular, for convective conditions, many particles would be brought down to the surface much faster by the convective downdrafts in the PBL. Thus, to account for turbulent processes, we propose to use the intensity of turbulence (I_t) in the estimation of sedimentation velocity, and we refer to it as the effective sedimentation velocity and it can be written as:

$$V_{ge} = V_g(1 + I_t) = \left(\frac{gC_p d_p^2}{18\mu}\right) (1 + I_t) \quad (12)$$

where I_t can be estimated as

$$I_t = \frac{e_*}{U}$$

In the above equation U is horizontal windspeed. See Part-1 paper for more details about the I_t parameter where it was estimated and analyzed for a decadal time period. Since intensity of turbulence is applicable for all stability regimes in the PBL, Eq. 12 works for all conditions in the PBL. Intercomparison results of both V_g and V_{ge} will be presented in the Results section.

2.4 Introducing effective Stokes number (St_e)

Stokes number, also known as reference Stokes number, is an important non-dimensional parameter that characterizes particle motion in atmospheric flows. It is defined as ratio of particle response time scale to the characteristic time scale of the flow. In estimating these respective time scales, traditionally sedimentation velocity and friction velocity along with respective characteristic length scale are used. For smooth and vegetated surfaces, reference Stokes number can be, respectively, written as:

$$St = \frac{V_g u_*^2}{g} \text{ and } St = \frac{V_g u_*}{gA} \quad (13)$$

where g is acceleration due to gravity, ν is kinematic viscosity of air, and A is characteristic radius of collectors. Note that friction velocity and hence reference Stokes number by themselves are only applicable for neutral conditions in the PBL while e_* is a better representation of the flow field's turbulence. Thus, we propose a new Stokes number, referred to as effective Stokes number (St_e), that includes the new velocity scale that works for different stability regimes in PBL. Then, St_e can be estimated by using Eq. 13 as:

$$St_e = \frac{V_{ge} k^2 e_*^2}{g} = \frac{(1+I_t)V_g k^2 e_*^2}{g} \text{ and } St_e = \frac{V_{ge} k e_*}{gA} = \frac{(1+I_t)V_g k e_*}{gA} \quad (14)$$

It is important to note that the new effective Stokes number works for different stability conditions in the PBL and is identically same as Stokes number for neutral conditions. Intercomparison results of Eq. 13 and 14 will be presented in the Results section.

2.5 Particle dry deposition formulations

In this section we describe two different particle deposition schemes and also respective new schemes that include 3-D turbulence effects. These two particle deposition schemes are suggested by (1) Zhang et al. (2001): referred to as Z01 scheme and the newly proposed scheme based on it is referred to as C01, and (2) Shu et al. (2021): referred to as S21 and the newly proposed scheme based on it is referred to as C21.

2.5.1 The Z01 and C01 schemes

The particle deposition scheme proposed by Zhang et al. (2001) has been used by regional and global chemical transport models (e.g., CAMx and GEOS-Chem). Here we present both the original scheme formulations as well as the proposed

new resistance formulations that include the new turbulence parameters. Z01 write particle size-dependent deposition velocity (V_d) as:

$$V_d = V_g + \frac{1}{R_a + R_b} \quad (15)$$

where V_g is sedimentation velocity, R_a and R_b are the aerodynamic resistance for heat and boundary layer (quasi-laminar sublayer) resistance, respectively. The aerodynamic resistance (R_a) for heat in the Z01 scheme is written as:

$$R_a = \frac{1}{ku_*} \left(\ln \left[\frac{z_r}{z_0} \right] - \Psi_H \right) \quad (16)$$

where k is von Karman constant, u_* is friction velocity, z_r is the height at which dry deposition velocity is evaluated, z_0 is surface roughness length, and Ψ_H is stability function for heat. Since buoyancy and shear production forces are included in the estimation of turbulence velocity, Alapaty et al. (2022) has proposed and validated a new formulation for R_a as:

$$R_a = \frac{1}{e_* k^2} \ln \left[\frac{z_r}{z_0} \right] \quad (17)$$

Since the above equation will work seamlessly for different stability regimes in the PBL, there is no need for explicitly using a stability function, a unique feature to avoid the options to choose from a wide selection of stability functions reported in the literature.

Resistance to transport through the very thin viscous sub-layer at the surface, R_b , is referred to as the quasi-laminar layer, laminar deposition layer or boundary layer (e.g., Pleim and Ran, 2011) where transport is fundamentally characterized by molecular diffusion for gases. For this reason, u_* is used traditionally in all such formulations without any stability correction parameters, like in Z01 scheme (Eq. 18). However, this is valid only for neutral conditions. During turbulent periods, such as daytime with surface heating, the literature indicates the presence of convective plumes at the leaf scale under still and windy air conditions since plants are subjected to heat load or thermal stress. Convection phenomena from plants in calm and windy air was observationally studied firstly by Gates and Benedict (1962). Using Schlieren photography and other instruments along with an infrared radiation gun, they quantitatively estimated the amount of energy convected away from a leaf under free and forced convection for broad-leaved and coniferous tree needles. Schlieren photography movies showed distinct convective plumes moving away from leaf surface indicating turbulence. In another experimental study, Wigley and Clark (1974) determined the heat transfer from model leaves heated by a constant energy flux under forced convection. In another experimental and field study, Brenner and Jarvis (1995) found that for forced convection conditions, at wind speeds above 2.5 m s⁻¹ leaf boundary layer conductances were higher than those for a laminar leaf boundary layer. As mentioned above, Wesely et al. (1985) have already introduced convection factor to improve turbulence effects. Considering results from these studies, we justify using the product ke_* in the place of u_* in the boundary layer resistance formulation. The boundary layer resistance (R_b) in

the Z01 scheme can be written as:

$$R_b = \frac{1}{\varepsilon_0 u_* (E_B + E_{IM} + E_{IN}) R_1} \quad (18)$$

where ε_0 is empirical constant set to 3, E_B , E_{IM} , and E_{IN} are the collection efficiencies from Brownian diffusion, impaction, and interception, respectively, and R_1 is correction factor to represent fraction of particles that stick to the underlying surface and is a function of Stokes number (St), which is also a function of land use. Here, R_1 is estimated as:

$$R_1 = e^{-\sqrt{St}} \quad (19)$$

The collection efficiencies are estimated as:

$$E_B = S_c^{-\gamma} \quad (20)$$

$$E_{IM} = \left(\frac{St}{\alpha + St} \right)^2 \quad (21)$$

$$E_{IN} = \frac{1}{2} \left(\frac{d_p}{A} \right)^2 \quad (22)$$

where S_c is ratio of kinematic viscosity of air to the Brownian diffusivity and is constant that varies as a function of land use and γ is a constant for each land use, d_p is particle diameter, and A is characteristic radius of collectors. Since we have defined the effective Stokes number, E_{IM} will also become a new equation because of the usage of Eq. 14. For finer details of original equations, readers are referred to Zhang et al. (2001).

In Z01 scheme, the R_b formulation (Eq. 18) has a global constant parameter (ε_0), which was set to 3. However, this formulation originated from Slinn (1982) in which ε_0 was defined as the ratio of friction velocity to the surface wind speed (U). Though it was neither stated nor recognized, this ratio is the intensity of turbulence as defined earlier, and was written as $\varepsilon_0 = u_* / U$. Then, the product of ε_0 and u_* in the denominator of Eq. 18 becomes aerodynamic resistance for neutral conditions. When we tested this original R_b formulation from Slinn (1982) in our single-point model, it resulted in unrealistically small (large) boundary layer conductances (resistances), particularly during daytime since aerodynamic conductance (resistance) is larger (smaller) during daytime (see Figure S1 in supplementary information). Potentially, for this reason Z01 might have introduced a global constant factor 3 in the place of ε_0 to achieve better performance. To relax this issue with the R_b estimation, we propose a two-step revision: (1) replace u_* with ke_* , and (2) replace the ε_0 with the turbulence factor, $(1+T_f)$, along with replacing u_* with ke_* . Then, using Eq. 4 and 6 in Eq. 18, the new R_b formulations can be written as:

$$R_b = \frac{1}{\varepsilon_0 ke_* (E_B + E_{IMe} + E_{IN}) R_{1e}} \quad (23a)$$

$$R_b = \frac{1}{(1+T_f) ke_* (E_B + E_{IMe} + E_{IN}) R_{1e}} \quad (23b)$$

where

$$R_{1e} = e^{-\sqrt{St_e}} \quad (24)$$

$$E_{IMe} = \left(\frac{St_e}{\alpha + St_e} \right)^2 \quad (25)$$

2.5.2 The S21 and the new C21 Schemes

Formulations of Shu et al. (2021), referred to as S21 (See Text S2 in supplementary information), are based on Pleim and Ran (2011) where S21 added a new term to R_b to calculate leaf area index (LAI)-dependent vegetative surface uptake. S21 showed that the new formulation introduced a vegetation dependence that is directionally consistent with the observed impact of vegetation on particle dry deposition and this update has resulted in relatively better results in the estimation of particle dry deposition. The R_a , and R_b equations used in S21 are written as:

$$R_a = 0.95 \frac{\ln\left(\frac{z_R}{z_0}\right) - \Psi_H}{ku_*} \quad (26)$$

$$R_b = \left[(1 + f_{veg}(max(LAI - 1, 0)))(1 + W_f) \bullet u_* (E_B + E_{IM}) \right]^{-1} \quad (27)$$

$$\text{and } W_f = 0.24 \frac{w_*^2}{u_*^2}$$

where f_{veg} is the fractional area of vegetation surface in a grid cell, which was introduced in the original R_b equation of Pleim and Ran (2011) in which they made a notable choice to ignore the interception term (E_{IN}) in the Eq. 27. In their scheme, dry deposition is estimated as:

$$V_d = \frac{V_g}{1 - e^{-(R_a + R_b)V_g}} \quad (28)$$

and sedimentation velocity equation used in Eq. 28 is same as that in Eq. 11.

Using the new velocity scale (Eq. 4) and turbulence factor (Eq. 10), we propose that the new equations for R_a , R_b , and V_d are written as:

$$R_a = 0.95 \frac{\ln\left(\frac{z_R}{z_0}\right)}{k_*^2 e_*} \quad (29)$$

$$R_b = \left[(1 + f_{veg}(max(LAI - 1, 0)))(1 + T_f) \bullet ke_* (E_B + E_{IMe}) \right]^{-1} \quad (30)$$

$$V_d = \frac{V_{ge}}{1 - e^{-(R_a + R_b)V_{ge}}} \quad (31)$$

As mentioned earlier, the T_f was estimated using bulk boundary layer parameters that are related to micrometeorological variables, 3-D variances of velocity fluctuations.

2.6 Single-point model

Numerical model used in this study is the same single-point model (DepoBoxToolv1.0) that was used by Shu et al. (2021) to test different particle dry deposition schemes for different land use. DepoBoxToolv1.0 was configured as an open-source Python tool, which can be easily modified to incorporate updates on the dry deposition schemes. All the deposition schemes were built into

Models.py file, basic functions were configured in functions.py file, and land category definition and parameterization were set in eval_luc.py file. DepoBox-Toolv1.0 has been freely available to the research community and the source code and required model inputs can be downloaded from the GitHub source (<https://github.com/shumarkq/DepoboxTool/tree/master>) and Zenodo open data repository (<http://doi.org/10.5281/zenodo.4749636>).

2.7 Measurements

As mentioned in the Introduction section, there are huge data gaps for particle measurements that include meteorological measurements. Thus, given the requirements for model inputs to perform single-point model simulations, we could find only 3 data sets. Of these three data sets, dry deposition measurements documented by Vong et al. (2004) indicated a bi-modal distribution for deposition velocity and such a variability cannot be well simulated by a single-point model since these types of models typically do not consider advective processes or cloud processes affecting deposition velocity. The second data set documented by Lamaud et al. (1994) for a coniferous site has data less than 12 hours and thus may not provide a statistically meaningful analysis and thus we excluded these two data sets. Thus, we have chosen the third data set, a field experiment at a forest site of the foothills of Mt. Asama in central Japan was conducted during July 2-8, 2009 (5.5 days -132 data points) and this site is characterized as alpine forest. Its canopy is dominated by the birch and alder tree species. During the study $PM_{2.5}$ sulfate fluxes were estimated as product of four-hour averaged transfer velocity between two measurement heights (21 and 27 m) and concentration difference at these heights. For this reason, estimated deposition velocities represent averaged values for six time periods: 0600-1000, 1000-1400, 1400-1800, 1800-2200, and 2200-0200 local time (LT) and they also assumed nighttime fluxes do not vary. Meteorological instruments and ultrasonic anemometer were placed at 28 m AGL using which various measurements were made. Here we briefly mention a few details and for specific details, readers are referred to Matsuda et al. (2010). All measurements included local time, air temperature, pressure, relative humidity, leaf area index, horizontal wind speed, friction velocity, canopy height, zero-plane displacement height, roughness length, measurement height, Monin-Obukhov length, and deposition velocity. The convective velocity was unavailable and thus was extracted from Weather Research and Forecasting (WRF) Model as documented in Shu et al. (2021). These measurements are used to provide needed inputs to the single-point model to simulate various deposition processes used in the estimation of particle dry deposition velocity.

2.8 Numerical simulations

Sulfate particle density was set as $\rho_p = 1500 \text{ kg m}^{-3}$, and the PSD was characterized by mass median diameter ($d_{pg} = 0.48 \text{ }\mu\text{m}$), and geometric standard deviation ($\sigma_g = 1.7$). As the PSD parameterization in the model may significantly impact the simulation results of particle deposition velocity, we followed the methods used by Shu et al. (2021) where the PSD was assumed to be dis-

crete size bins for Z01, C01, S21, and C21 schemes with 100 bins (See Text S3 in supplementary information) and continuous log-normal distribution for S21 and C21 schemes. The log-normal distribution of the particle size as defined by d_{pg} and σ_g and the single-point model integrates across the whole particle size range using the modal integration formulations (See Text S4 in supplementary information). We reiterate that PSD data was not available and thus the chosen PSD may not be representative of actual size distribution that was not measured. Three schemes that used sectional approach to perform numerical simulations are referred to as: Z01-B, C01-E, and C01-ETF, where Z01-B refers to base scheme, C01-E represents base scheme using e_* (turbulence velocity scale), and C01-ETF represents base scheme using e_* as well as the turbulence factor. The S21 and C21 schemes are configured to use sectional as well as modal approaches and thus S21-BS and S21-BM represent base scheme using sectional and modal approaches, while C21-ETFS and C21-ETFM represent base scheme using e_* as well as the turbulence factor with sectional and modal approaches, respectively. Detailed information about all equations used in Z01, S21, C01, and C21 can be found in the Table 1 and Table 2 shows a list of all simulations performed and differences between each simulation. Model simulations were performed for 132 hours for each of the seven cases described above.

Table 1. Equations used to represent several processes in each of the schemes

Scheme	Single Di- ame- ter	Modal ap- proach	Sectional ap- proach	V_d	V_g or V_{ge}	R_a	R_b	E_B	E_{IM}	E_{IN}	St		
Z01- B				$V_g + \frac{1}{R_a + R_b}$	$\frac{\rho d_p^2 g C}{18\eta}$	$\frac{\ln(\frac{z_R}{z_0}) - \Psi_H}{ku_* \varepsilon_0 u_* (E_B + E_{IM} + E_{IN})}$	$\frac{St}{(1+T_f)ke_*}$	$\frac{St}{E_B + E_{IM} + E_{IN}}$	$\frac{St}{(1+T_f)ke_*}$	$\frac{St}{E_B + E_{IM} + E_{IN}}$	$\frac{\beta}{2} \left(\frac{d_p}{A}\right)^2 \frac{V_g u_*}{gA}$	NA	Yes
C01- E				$V_{ge} + \frac{1}{R_a + R_b}$	$\frac{\rho d_p^2 g C}{18\eta} \left(1 + \frac{\ln(\frac{z_R}{z_0})}{k^2 e_*}\right)$	$\frac{\ln(\frac{z_R}{z_0}) - \Psi_H}{\varepsilon_0 ke_* (E_B + E_{IM} + E_{IN})}$	$\frac{St}{(1+T_f)ke_*}$	$\frac{St}{E_B + E_{IM} + E_{IN}}$	$\frac{St}{(1+T_f)ke_*}$	$\frac{St}{E_B + E_{IM} + E_{IN}}$	$\frac{\beta}{2} \left(\frac{d_p}{A}\right)^2 \frac{V_{ge} ke_*}{gA}$	NA	Yes
C01- ETF				$V_{ge} + \frac{1}{R_a + R_b}$	$\frac{\rho d_p^2 g C}{18\eta} \left(1 + \frac{\ln(\frac{z_R}{z_0})}{k^2 e_*}\right)$	$\frac{\ln(\frac{z_R}{z_0}) - \Psi_H}{(1+T_f)ke_* (E_B + E_{IM} + E_{IN})}$	$\frac{St}{(1+T_f)ke_*}$	$\frac{St}{E_B + E_{IM} + E_{IN}}$	$\frac{St}{(1+T_f)ke_*}$	$\frac{St}{E_B + E_{IM} + E_{IN}}$	$\frac{\beta}{2} \left(\frac{d_p}{A}\right)^2 \frac{V_{ge} ke_*}{gA}$	NA	Yes

Single Di- ame- ter	Modal	Sectional
S21- B	$\frac{V_g \rho d_p^2 g C}{1 - e^{-V_g (R_a + R_b)}}$	$0.95 \frac{\ln(\frac{Z_R}{Z_0}) - \Psi_H}{k u_*} \mathcal{C}_{eg}^{-\frac{2}{3}} \max(\frac{St_e^2}{1 + St_e}, NA, 0) \left(\frac{V_{ge} u_*}{gA} + 0.04 \frac{w_*^2}{u_*^2} \right) \bullet \mathcal{C}_{eg} (E_B + E_{IM}) \Big]^{-1}$
	as- sume 0	\widehat{V}_g \widehat{E}_{IM} $\widehat{E}_{IM} = \frac{\widehat{St}^2}{1 + \widehat{St}}$ $\widehat{St} = \frac{\widehat{V}_g u_*}{gA}$
C21- ETF	$\frac{V_{ge} \rho d_p^2 g C}{1 - e^{-V_{ge} (R_a + R_b)}} \frac{\ln(\frac{Z_R}{Z_0})}{\kappa^2 L_e} (1 + \mathcal{C}_{eg}^{-\frac{2}{3}} \max(\frac{St_e^2}{1 + St_e}, NA, 0)) \left(\frac{V_{ge} ke_*}{gA} + T_f \right) \bullet ke_* (E_B + E_{IME}) \Big]^{-1}$	I_t
	as- sume 0	\widehat{V}_{ge} \widehat{E}_{IM} $\widehat{E}_{IM} = \frac{\widehat{St}^2}{1 + \widehat{St}}$ $\widehat{St} = \frac{\widehat{V}_{ge} ke_*}{gA}$

Table 2 Description of schemes used in model simulations

Scheme	Description
Z01-B	Base Z01 scheme
Z01-E	Base Z01 scheme using e_*
Z01-ETF	Base Z01 scheme using and e_* and T_f
S21-BS	Base S21 scheme (sectional)
S21-BM	Base S21 scheme (modal)
C21-ETFS	Base S21 scheme using and e_* and T_f (sectional)
C21-ETFM	Base S21 scheme using and e_* and T_f (modal)

2.9 Metrics used for evaluation

The evaluation of the newly proposed particle dry deposition schemes was performed via comparison to the measured particle deposition velocities. Following the approaches by Chang and Hanna (2004) and Emery et al. (2017), three metrics including fractional bias (FB), normalized mean error (NME), and Pearson correlation coefficient (R) were used to evaluate the performance of the model formulations. Associated parameter descriptions are as follows: the overbar means averaging, the bracket means averaging, V_o and V_p denote measured and predicted deposition velocities, and subscript i indicates the paired V_o and V_p .

$$\text{FB} = \frac{2 \times ([V_p] - [V_o])}{[V_o] + [V_p]}$$

$$\text{NME} = \frac{\sum |V_{p,i} - V_{o,i}|}{\sum V_{o,i}}$$

$$\text{R} = \frac{\sum [(V_{p,i} - \bar{V}_p) \times (V_{o,i} - \bar{V}_o)]}{\sqrt{\sum (V_{p,i} - \bar{V}_p)^2 \times \sum (V_{o,i} - \bar{V}_o)^2}}$$

3 Results and Discussions

Firstly, we present the results for the estimation of intensity of turbulence, effective sedimentation velocity, effective Stokes number, and turbulence factor that we introduced in the Section 2. Then, we present results obtained from Z01-B, C01-E and C01-ETF and then from S21 and C21 formulations. As mentioned earlier, since fluxes are estimated for each time interval of four hours, consistently we present results for those time intervals in the temporal variation figures. Thus, data from model simulations for all days (e.g., 5.5 days) are grouped according to those six time intervals and then for each time interval median value is generated and used in the following figures, consistent with the original analysis of Matsuda et al. (2010). In addition, we also show hourly temporal variation of hourly averages for various results.

3.1 Characterization of turbulence parameters

Figure 1a and 1b show diurnal variation of median and hourly averaged e_* , horizontal wind speed (U), and intensity of turbulence, I_t . Since e_* includes the contribution by the surface sensible heat flux to the turbulence, during daytime it shows a variability typical of heat flux and thus usage of e_* should have an impact on the resistances estimation equations used to estimate deposition velocity. Since I_t varies from 0 to about 1, usage of I_t in equations for sedimentation velocity and Stokes number will not only introduce diurnal variability but also an increase in magnitudes of such estimations. It can be seen that trends in measured wind speeds are higher during nighttime than during daytime reflecting trends in e_* during nighttime, as expected as per the e_* formulation. Measured horizontal wind speed is noisy showing oscillations (Fig 1b) in time and is responsible for such oscillations in e_* during nighttime while during daytime such oscillations are suppressed by the dominant contribution by the w_* term in the e_* estimation. Similar oscillations can be found only during daytime in the I_t estimation and absence of such oscillations may be due to cancellation effects.

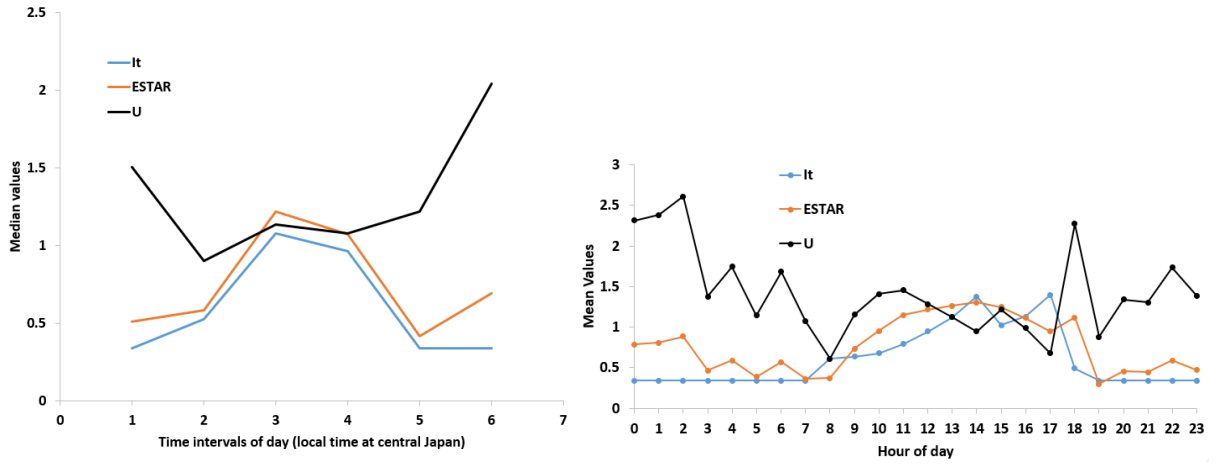


Figure 1. Diurnal variation of (a) median and (b) hourly averaged intensity of turbulence, turbulence velocity scale, and horizontal wind speed.

Diurnal variation of median and hourly averaged observed u_* and the estimated e_* is shown in Figure 2. Reported values of u_* are confined between 0.2 and 0.3. Thus, usage of u_* without utilizing a stability function can underrepresent turbulence magnitude in process formulations. This is where the advantage of using e_* lies in, *i.e.*, no need to use a stability function since it includes the effects of surface sensible heat flux on the turbulence and thus responsible for large diurnal variation. We have demonstrated in our companion paper (Part-1) that the product of k and e_* can successfully replace u_* measured by 3-D sonic anemometer (that includes surface heat flux contribution) in several resistance formulations, producing realistic ozone deposition fluxes and deposition velocities. In this study also, temporal variation of the product k and e_* , shown in Figure 2, also has a typical diurnal variation which is a signature of many boundary layer parameters. Error bars (Fig. 2a) indicate variability within ± 1 standard deviation.

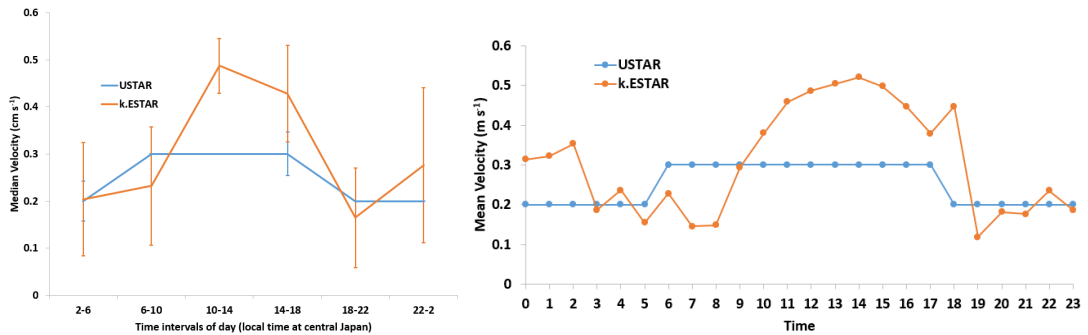


Figure 2. Diurnal variation of (a) median and (b) hourly averaged USTAR and $k \cdot e_*$.

friction velocity and product of von Karman constant and turbulence velocity scale.

Figure 3a and 3b show diurnal variation of median and hourly averaged sedimentation velocity and effective sedimentation velocity using Eq. 11 and 12. As expected, for the chosen particle diameter ($0.48 \mu\text{m}$), sedimentation velocity is constant and is independent of time as reflected in the Fig. 3. However, with the usage of I_t , turbulence effects are reflected in the effective sedimentation velocity estimation, showing a diurnal variation typical of certain boundary layer parameters during warmer days. The third force, namely, the turbulence is included in Eq. 12 and thus effective sedimentation velocity seems to be a good choice representing effects of turbulence on particle deposition. We find that the maximum median V_{ge} is about 2 times that of V_g and for all days of simulation V_{ge} has been always higher than V_g irrespective of PBL stability regimes. Since wind-related oscillations are induced in the estimation of I_t , and I_t is used in V_{ge} estimation, it has resulted in oscillations (Fig. 3b).

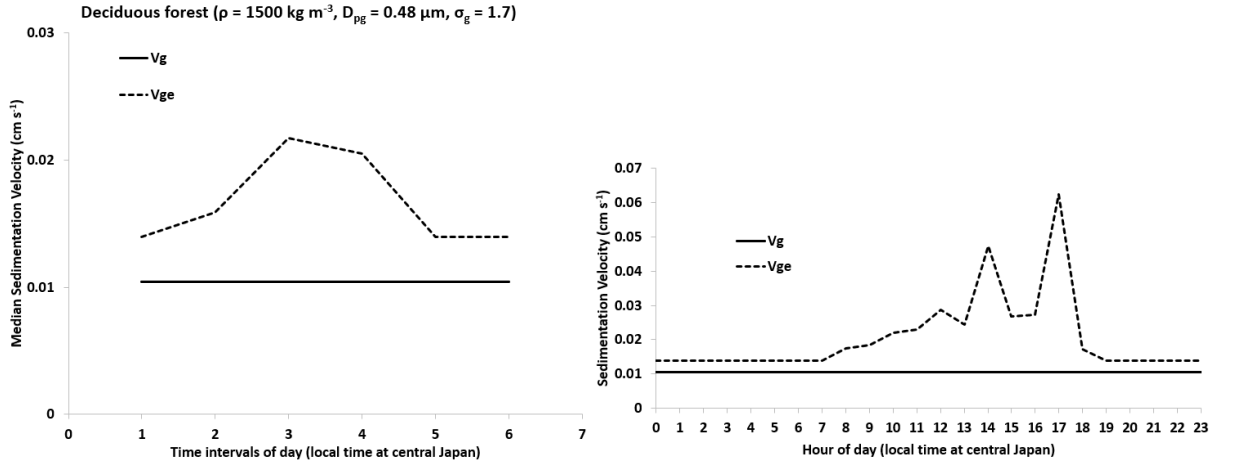


Figure 3. Diurnal variation of median sedimentation and effective sedimentation velocity.

Figure 4a shows diurnal variation of estimated median reference Stokes number (St) and median effective Stokes number (St_e) using Eq. 13 and 14 for each time interval. Variability for the St is solely dictated by the variation of u_* since other parameters used in Eq. 13 are constant in time. However, St_e estimation is controlled by both the V_{ge} and e_* and thus the net impact of these parameters has introduced increased diurnal variability accounting for diurnally varying turbulence. As a result, the maximum median and hourly averaged St_e is about 3 and 7 times higher than that of St . Further, St_e is always higher than that St for all PBL conditions. Since boundary layer resistance estimation depends on the magnitude of Stokes number, its magnitude will also be affected. Again, oscillations (Fig. 4b) in St are originating from that present in the wind

speed measurements.

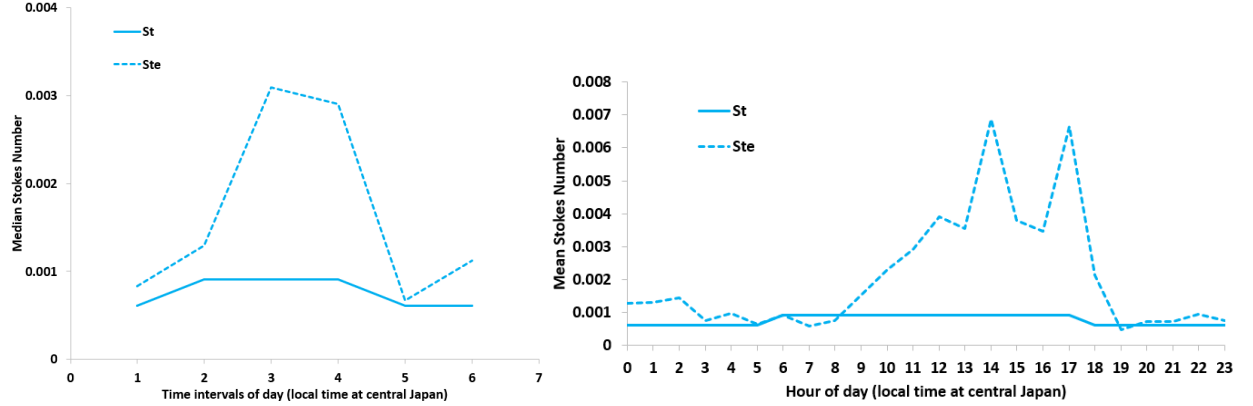


Figure 4. Diurnal variation of (a) median and (b) hourly averaged reference Stokes number and effective Stokes number.

Figure 5 shows diurnal variation of median and hourly averaged turbulence factors (T_f and W_f) estimated using Eq. 5 and 10. To the best of our knowledge, temporal variation and magnitude of W_f was neither compared with nor evaluated against other similar turbulence factor estimates and thus our new formulation fills this scientific gap. Saylor et al. (2019) have shown that depending up on the magnitude of convective velocity (w_*), estimated dry deposition can differ by as much as about 10 times when using Eq. 5. Though our new turbulence factor (Eq. 10) also uses w_* , our e_* equation (Eq. 3) that we proposed was validated using the 3-D micrometeorological data for a decadal period (see Part-1 for more information) and thus offers a good level of confidence in using Eq. 10. Both equations (5 and 10) differ in complexity and Eq. 5 only works for convective boundary layers while Eq. 10 works for all stability regimes in the PBL. Thus, for time intervals 1, 5, and 6 (i.e., hours 0200-0600, 1800-2200, and 2200-0200) and nighttime in Fig. 5a and 5b W_f is set to zero while T_f is non-zero by design. Thus, during nighttime, R_b estimations using T_f will be lower as compared to that using W_f . During convective conditions, maximum difference between T_f and W_f occurs at time interval 2 and that difference reduces to about 0.2 until PBL regime switches to stable conditions at time interval 5. This feature of T_f is similar to generally observed rapid growth of PBL during morning hours in warmer days. Finally, T_f is always higher than W_f and thus turbulence effects are stronger in formulations where T_f is used as compared to that with W_f and these effects will be relatively stronger with using T_f during stable conditions as compared to convective conditions in PBL. In this case study, two very different formulations yielded very similar results for convective conditions. However, when we estimated T_f and W_f using the Harvard Forest site data for a decadal period (not shown), we found that T_f is always higher by about 2 times than the W_f with magnitude ranges between about 1 to 10.

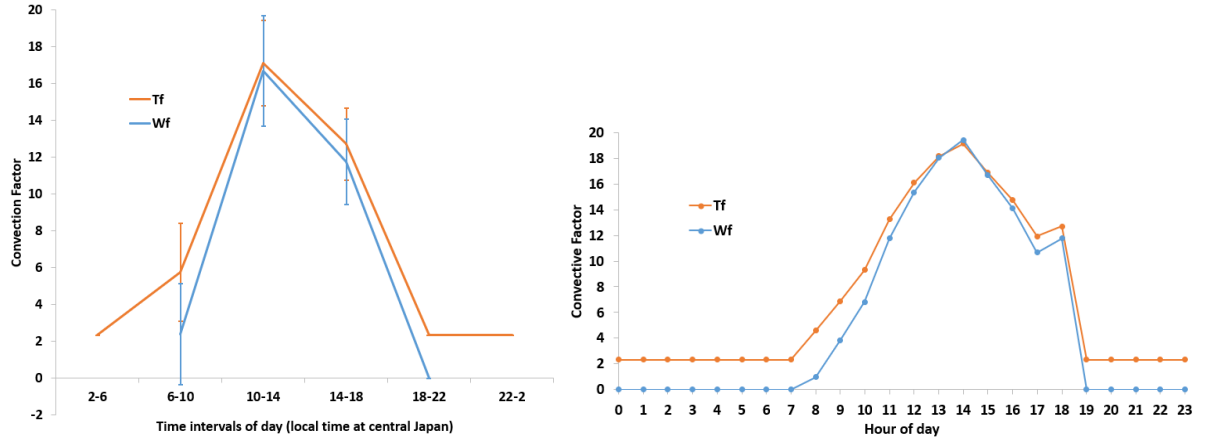


Figure 5. Diurnal variation of turbulence factors.

3.2 Simulation Results from Z01 and C01 formulations

Single-point model simulation results from Z01-B, C01-E, and C01-ETF are presented in this section, which are based on sectional mode of PSD. In addition to the temporal distributions of V_d , its components' distribution will also be shown here to explore the difference between these cases. Figure 6 shows the median and hourly averaged deposition velocities (V_d), estimated (referred to as measured and OBS) from using 4-hour averaged aerosol flux and transfer velocity measurements and corresponding model simulations for Z01-B, C01-E, and C01-ETF. V_d for OBS ranges from about 0.2 to 1 cm s^{-1} with maximum occurring at time interval 3 (1000 to 1400 LT). In general, all schemes underestimated V_d when compared to corresponding measured

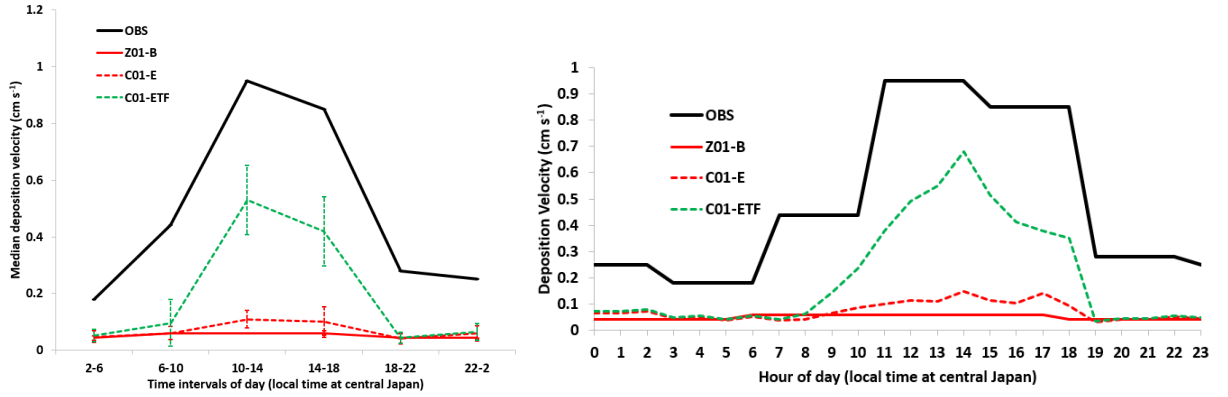


Figure 6. Diurnal variation of estimated median and hourly averaged dry deposition velocity from measurements and model simulations for Z01-B, C01-E, and C01-ETF.

V_d values, which are significantly higher during daytime than nighttime due to

convective conditions in PBL. Both Z01-B and C01-E didn't capture strong diurnal variation found in measured V_d though they both have a very weak diurnal variability. However, Z01-ETF predicted relatively stronger diurnal variation with higher deposition velocities during daytime, but maximum median (hourly averaged) V_d is about 50% (40%) smaller to that of measured maximum. During nighttime Z01-ETF has slightly higher V_d compared to other two cases because the turbulence factor that works for both day and night, however, V_d is still lower than measured values. Thus, even with increased turbulence representation in C01-ETF, estimated V_d is much underpredicted and thus it seems that there are opportunities to improve processes representation in the Z01 scheme, and one type of improvements were demonstrated by Emerson et al. (2020).

Modeled V_d is the sum of V_g and the conductance through R_a and R_b , thus, these parameters can contribute to diurnal variations of V_d with higher V_d during the daytime. Specifically, for Z01-B, Figure 3 indicated no diurnal variation for V_g and thus the very small diurnal variation of V_d can only be attributed to conductance through R_a and R_b while

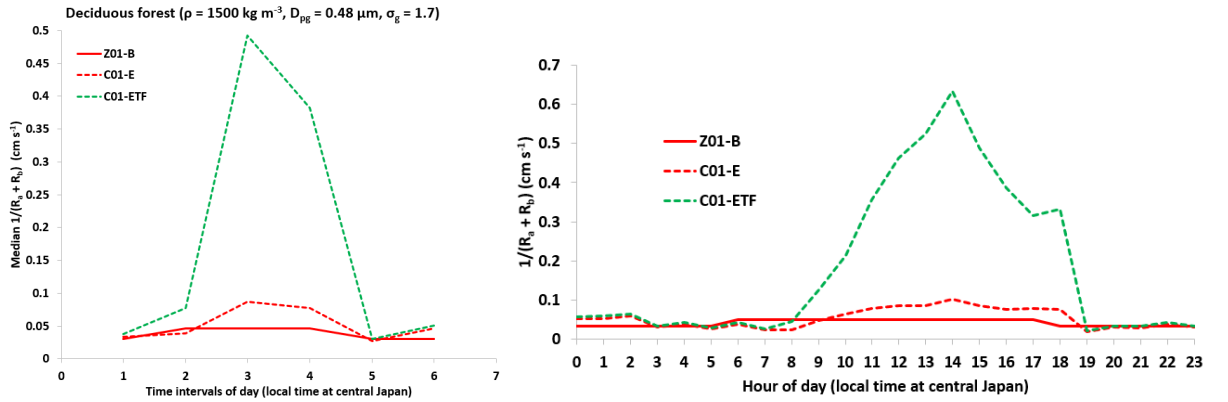


Figure 7. Diurnal variation of median and hourly averaged total conductance for Z01-B, C01-E, and C01-ETF.

for C01-E and C01-ETF diurnal variation of V_{ge} has also contributed to diurnal variation of V_d . The total conductance showed in Figure 7 for Z01-B has negligible diurnal variation since u_* is the only parameter that can induce diurnal variability but as u_* has a weak diurnal variation it has resulted in such weak temporal variability in total conductance. Since C01-E uses e_* , it fared little better than Z01-B but with much smaller diurnal range as compared to C01-ETF.

Figure 8 shows temporal variation of median and hourly averaged boundary layer conductance, and it is largely similarly to the total conductance shown in Fig. 7. This result implies that the boundary layer resistance is controlling the pattern and magnitude of V_d . It is interesting to note that the introduction of turbulence factor (T_f) has increased boundary layer conductance in C01-

ETF by about 5 times that of the C01-E and thus have contributed to the improved estimation of V_d . Thus, the incorporation of e_* and T_f into the Z01 scheme equations resulted in the better model performance of estimating V_d . Comparison of simulated aerodynamic conductance is presented in the next section along with other cases.

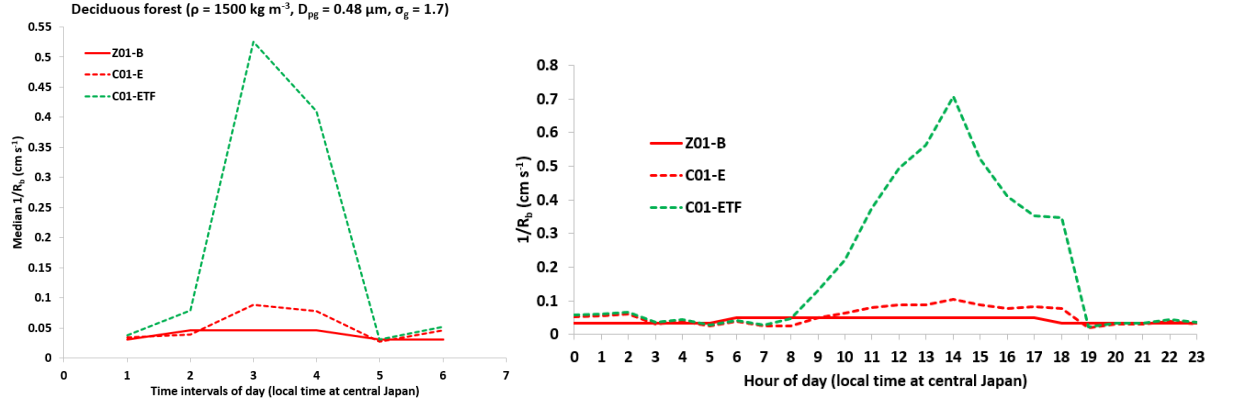


Figure 8. Diurnal variation of median and hourly averaged boundary layer conductance for each time interval for Z01-B, C01-E, and C01-ETF.

3.3 Simulation results from S21 and C21 formulations

In addition to S21 and C21 schemes' performance analysis, we also include the results from C01-ETF since it has the best performance among all other schemes considered in the previous Section. Figure 9 shows temporal variation of median and hourly averaged deposition velocities from OBS and corresponding simulations by C01-ETF, S21-BS, C21-ETFS, S21-BM, and C21-ETFM. At the outset, it can be seen that the C21 scheme (i.e., C21-ETFS and C21-ETFM) performed better than all other 3 schemes (i.e., C01-ETF, S21-BS, and S21-BM). The minor differences between simulated V_d for sectional and modal approaches of S21 and C21 schemes can be attributed to the type of representation of aerosol size distribution methodologies used in this study. It is also interesting to note that C01-ETF performed better than the S21-BS and S21-BM and the improved performance of C01-ETF may be attributed to the fact that it includes newly introduced turbulence parameters. All schemes underestimated V_d during nighttime while C21 schemes performed marginally better than other schemes.

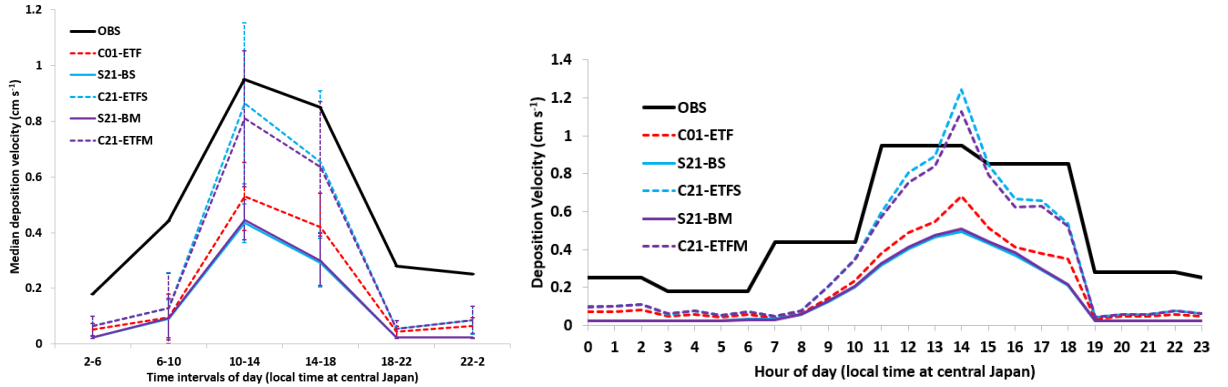


Figure 9. Diurnal variation of estimated median and hourly averaged dry deposition velocity from measurements and model simulations for C01-ETF, S21-BS, C21-ETFS, S21-BM, and C21-ETFM.

To further analyze contributions by various processes in the estimation of V_d , we show temporal variation of median total conductance for all cases in Figure 10. Since contribution by sedimentation velocity is smaller compared to other terms in V_d estimation, total conductance magnitude and its temporal variation is very similar to that in V_d . To further probe into the relative contributions by each conductance, we show median and hourly averaged boundary layer and aerodynamic conductances temporal variation in Figures 11 and 12. It can be seen that boundary layer conductance for C01-ETF is slightly higher than that for S21 schemes while the aerodynamic conductance for C01-ETF is about two times higher than that for S21. As a result, V_d for C01-ETF has ended up slightly higher than that in S21 schemes. On the other hand, maximum median aerodynamic conductance (Fig. 12) for Z01 scheme is higher than that for all other schemes and it is directly attributed to the usage of a type of stability function for heat in the Z01 scheme (Eq. 16) while a different type of stability function is used in S21 and no stability function in C21 resulting in different estimations. This is one of the causes of differing outcomes from using different stability functions in the dry deposition modeling. Truly, it is one of the objectives of the Part-1 paper where we have introduced the e_* formulations to avoid using such stability functions and help to mobilize scientists towards the development of the community dry deposition modeling. The minor differences in the estimated median aerodynamic resistance in C01 and C21 is attributed to the usage of factor 0.95 in C21, since both use our e_* methodology.

Another characteristic present in the aerodynamic conductance estimations using Z01 and S21 schemes is that the maximum median aerodynamic conductance occurs at time interval 2 (0600 to 1000 LT) while for the C01 and C21 formulations the maximum occurs at time interval 3 (i.e., 1000 to 1400 LT). Usually, such maximum values, for clear warmer days like in this study, happens during mid-day but not in the morning. This result also points to the potential source of differing V_d estimations, which can result from using different stability

functions.

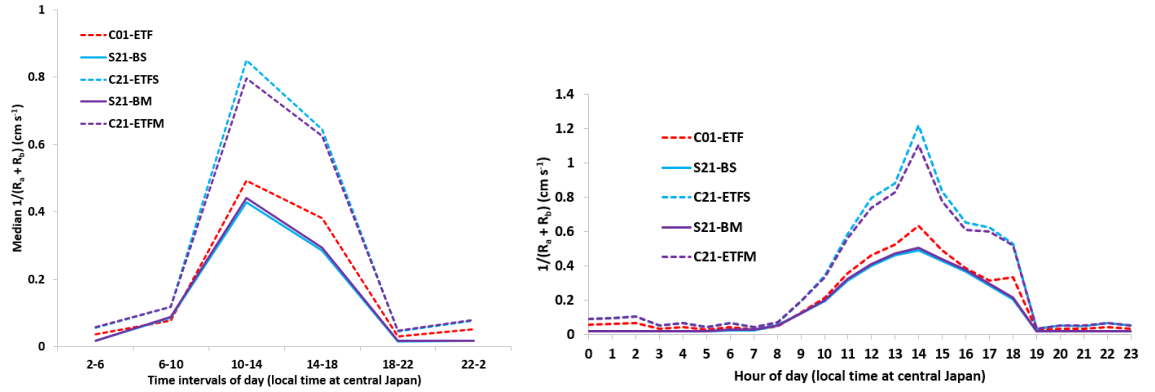


Figure 10. Diurnal variation of median and hourly averaged total conductance for C01-ETF, S21-BS, C21-ETFS, S21-BM, and C21-ETFM.

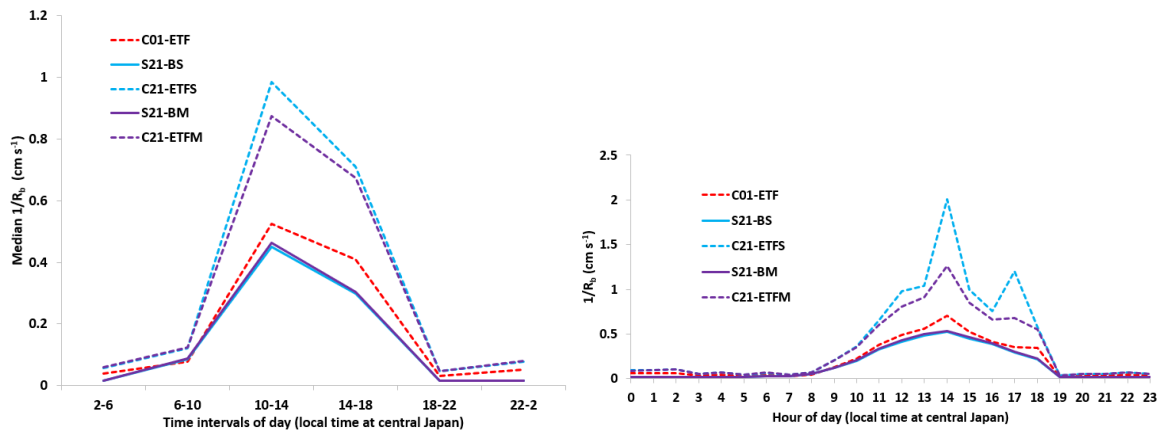


Figure 11. Diurnal variation of median and hourly averaged boundary layer conductance for C01-ETF, S21-BS, C21-ETFS, S21-BM, and C21-ETFM.

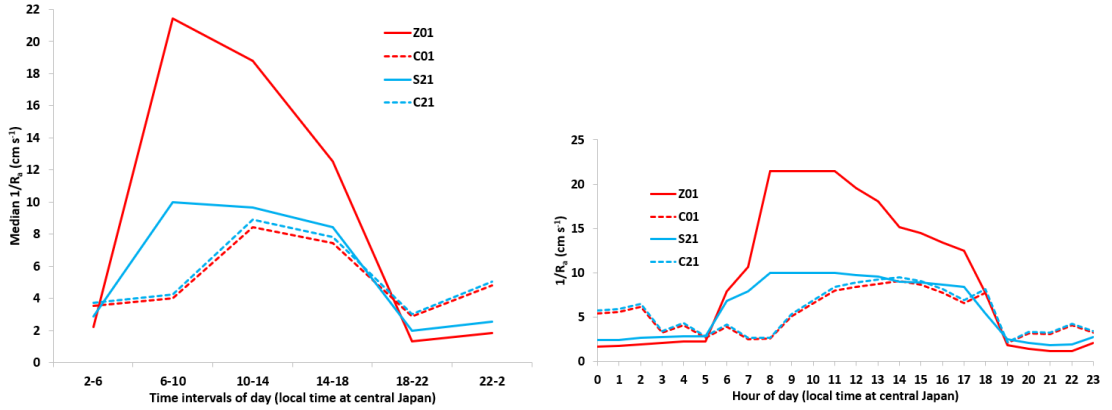


Figure 12. Diurnal variation of median and hourly averaged aerodynamic conductance for C01-ETF, S21-BS, C21-ETFS, S21-BM, and C21-ETFM.

To examine the differences in V_d simulated by various schemes with differing PSD, we simulated V_d curves integrated either by sectional (S) or modal (M) approach from seven deposition schemes (described previously) with three σ_g (1.01, 1.7, and 2.5). As shown in the Figure S2 in the supplementary information, the comparison of simulated V_d across schemes is not sigma-dependent because all schemes exhibit consistent patterns as σ_g changes. However, when σ_g is increased from 1.01 to 2.5, the V_d trends for all schemes shift to the left, bringing the minimum V_d from at 2 to 0.1 m. This characteristic change is expected, as reported in Shu et al. (2021). Due to the consistency of modeled trends at three σ_g values, we will choose $\sigma = 1.01$ to illustrate the outcomes of all schemes. For particles between 0.01 and 10 microns, C21-ETFS has the highest V_d (1.57-2.50 cm s⁻¹). Following C21-ETFS, another three schemes (C01-ETF, C21-ETFM, and S21-BS) have a relatively lower V_d (0.94-1.06 cm s⁻¹). These three schemes have the same V_d between 0.08 and 0.8 microns but begin to differ as particle size increases or decreases. C01-E, Z01-B, and S21-BM have the smallest V_d (0.34-0.58 cm s⁻¹), particularly between 0.01-2.5 microns, when compared to the other four schemes. Compared to their performance by category, C01-ETF, as modified versions of Z01-B, can predict higher V_d , whilst C01-E changes marginally. As a modified version of S21-B (S or M), C21-ETF (S or M) considerably increase V_d between 0.01 and 10 microns, which is consistent with diurnal evaluation results in previous sections. It is worth noting that the V_d predicted by the same scheme differs substantially after applying alternative PSD approaches (S or M). Between 0.01 and 2.5 microns, the V_d simulated by S21-B (S) and C21-ETF (S) using the sectional method are 1.80-2.56 and 1.11-1.36 times greater than that simulated by S21-B (M) and C21-ETF (M) using the modal approach.

To quantitatively show the differences in model performance for all cases, fractional bias, (FB), Pearson correlation coefficient (R), and normalized mean error

(NME) results are shown in Table 3.

Table 3. Model performance evaluation for all cases using median values as well as entire simulation data

Schemes	Median FB	Whole data FB	Whole data R	Whole data NME
Z01-B	-1.52	-1.61	0.67	0.89
C01-E	-1.42	-1.47	0.68	0.85
C01-ETF	-1.04	-0.84	0.91	0.59
S21-BS	-1.32	-1.07	0.94	0.70
C21-ETFS	-0.79	-0.43	0.88	0.43
S21-BM	-1.32	-1.05	0.94	0.69
C21-ETFM	-0.80	-0.48	0.89	0.44

Incorporation of turbulence velocity, intensity of turbulence, and new turbulence factor into resistances estimation, has improved the model performance in the estimation of particle deposition velocity and is reflected in the FB and NME estimations while R has shown slightly different metrics. Consistent with the results presented earlier, Table 3 indicates that all schemes underestimated deposition velocity leading to negative FB values. Median values as well as all modeled values used to estimate FB and NME indicate that C21-ETFS has performed the best followed by C21-ETFM while Z01-B the least. In the next section, we present results from a sensitivity simulation.

3.4 Sensitivity study

Based on the results presented in the above sections, it will be interesting to perform one more simulation to study impacts of using T_f in the place of W_f in S21-BS in the estimation of particle deposition and we refer to it as S21-BSTF. Since in this case study, in general, T_f is very similar to W_f in its magnitude and temporal variation during daytime (Fig. 5), one would expect that switching to T_f in S21-BS would not result in major improvements in V_d estimation by S21-BS. Figure 13 shows temporal variation of median V_d from OBS and S21-BS, C21-ETFS, and S21-BSTF. As expected, S21-BSTF has a minor improvement during convective conditions as compared to stable conditions but in general there is no significant improvement when compared to C21-ETFS and OBS. This result confirms a fact that major improvements in C21-ETFS came from improved representation of turbulence from introducing intensity of turbulence and turbulence velocity scale into the respective processes, i.e., effective sedimentation velocity and effective Stokes number.

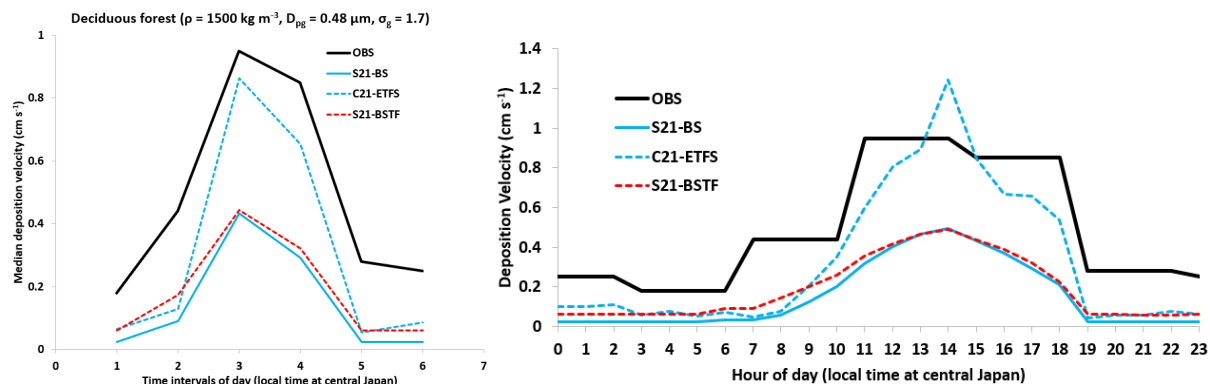


Figure 13. Diurnal variation of estimated median and hourly averaged dry deposition velocity from measurements and model simulations for S21-BS, C21-ETFS, and S21-BSTF.

4 Conclusions

We proposed four new deposition formulation schemes (i.e., C01-E, C01-ETF, C21-ETFS, and C21-ETFM) to model particle dry deposition with an aim to improve representation of turbulence in various deposition processes and intercompare model results with three existing schemes (i.e., Z01-B, S21-BS, and S21-BM). All these formulations were applied at a site characterized by deciduous forest using a single-point model. Numerical simulations were performed for 5.5 days, and model evaluation was performed using particle deposition velocities estimated from measurements available at the site. Notably, we improved turbulence representation in process via introducing three turbulence parameters: (1) a new turbulence velocity scale (e_*) in the place of friction velocity; (2) intensity of turbulence (I_t), and (3) a new turbulence factor (T_f). As a consequence, we have introduced effective sedimentation velocity and effective Stokes number that account for realistic representation of turbulence for conditions in the PBL.

Results indicate that new schemes performed better than existing schemes. Introduction of three turbulence parameters into the Z01 scheme significantly improved the model performance and predicted stronger diurnal variation of V_d though it still underpredicted V_d when compared to that estimated from measurements. We found that these three parameters either introduced or added more diurnal variability to processes and subprocesses during daytime due to the strong diurnal variability of these three turbulence parameters. In this case study, the best performing scheme was found to be C21-ETFS followed by C21-ETFM. As expected, results are barely sensitive to aerosol size distribution methodologies used in the study.

Though we improved representation of turbulence in these schemes, each scheme resulted in differing estimates of V_d for particle sizes that are of health concerns (i.e., $\text{PM}_{2.5}$). This result highlights an urgent need for required long term and

comprehensive meteorological and particle measurements for a systematic evaluation of each scheme that would help to recognize best performing formulations which in turn open doors for laying the foundations for the community particle deposition modeling framework. Without such comprehensive measurements, accurate particle deposition modeling will continue to be an elusive goal. In addition, fundamental understanding of particle dry deposition is still needed in the future to improve our ability to accurately model it. At least, findings from this research may help improve the capability of dry deposition schemes for improved estimation of particle dry deposition. Further testing of the new schemes in 3-D air quality model is needed, which will be the focus of our future studies and that effort would help to foster the development of the community deposition modeling system serving regional and global modelers.

Acknowledgments

The research was partially and internally funded by the U.S. EPA. Our sincere gratitude goes to Mr. John M. Southerland, Jr. for kindly supporting the research. We thank Drs. Christian Hogrefe, Benjamin Murphy, and Sergey Napelenok for their helpful comments. This work has been cleared for publication by the ORD and the views expressed and the contents are solely the responsibility of the authors and do not necessarily represent the official views or policies of the U.S. EPA.

Data and code availability

Model code and all the data used to generate figures and tables shown in this article can be freely downloaded at <http://doi.org/10.5281/zenodo.5874973>.

References

- Ahlm, L., Krejci, R., Nilsson, E. D., Mårtensson, E. M., Vogt, M., & Artaxo, P. (2010), Emission and dry deposition of accumulation mode particles in the Amazon Basin. *Atmospheric Chemistry and Physics*, 10(21), 10237–10253. <https://doi.org/10.5194/acp-10-10237-2010>
- Alapaty, K., Cheng, B., Bash, J., Munger, J. W., Walker, J. T., & Arunachalam, S. (2022), Dry deposition methods based on turbulence kinetic energy: Part 1. various resistances evaluation and sensitivity studies. *Journal of Geophysical Research: Atmospheres*, in review.
- Binkowski, F. S. & Shankar, U. (1995), The Regional Particulate Matter Model: 1. Model description and preliminary results, *Journal of Geophysical Research: Atmospheres*, 100(D12), 26191–26209. <https://doi.org/10.1029/95JD02093>
- Brenner, A. J., & Jarvis, P. G. (1995), A heated leaf replica technique for determination of leaf boundary layer conductance in the field. *Agricultural and Forest Meteorology*, 72(3–4), 261–275. [https://doi:10.1016/0168-1923\(94\)02160-L](https://doi:10.1016/0168-1923(94)02160-L)
- Chang, J. C., & Hanna, S. R. (2004), Air quality model performance evaluation. *Meteorology and Atmospheric Physics*, 87, 167–196. <https://doi.org/10.1007/s00703-003-0070-7>

- Emerson, E. W., Hodshire, A. L., DeBolt, H. M., Bilsback, K. R., Pierce, J. R., McMeeking, G. R., & Farmer, D. K. (2020), Revisiting particle dry deposition and its role in radiative effect estimates. *PNAS*, *117*(42), 26076–26082. <https://doi.org/10.1073/pnas.2014761117>
- Emery, C., Liu, Z., Russell, A. G., Odman, M. T., Yarwood, G., & Kumar, N. (2017), Recommendations on statistics and benchmarks to assess photochemical model performance. *Journal of the Air & Waste Management Association*, *67*(5), 582–598. <https://doi.org/10.1080/10962247.2016.1265027>
- Erismann, J. W., & Draaijers, G. P. J. (1995), *Atmospheric deposition in relation to acidification and eutrophication, studies in environmental science*, (Vol. 63. pp. 55–75). Netherlands: Elsevier.
- Farmer, D. K., Boedicker, E. K., & DeBolt, H. (2021), Dry deposition of atmospheric aerosols: approaches, observations, and mechanisms. *Annual review of physical chemistry*, *72*, 375–397. <https://doi.org/10.1146/annurev-physchem-090519-034936>
- Fowler, D., Pilegaard, K., Sutton, M. A., Ambus, P., Raivonen, M., et al. (2009). Atmospheric composition change: ecosystems–atmosphere interactions. *Atmospheric Environment*, *43*(33), 5193–267. <https://doi:10.1016/j.atmosenv.2009.07.068>
- Gates, D. M., & Benedict, C. M. (1962), Convection phenomena from plants in still air. *American Journal of Botany*, *50*(6), 563–573. <https://doi.org/10.2307/2440031>
- Hicks, B. B., Saylor, R. D., & Baker, B. D. (2016), Dry deposition of particles to canopies – A look back and the road forward. *Journal of Geophysical Research: Atmospheres*, *121*(24), 14691–14707. <https://doi:10.1002/2015JD024742>
- Hinds, W. C. (1999), *Aerosol technology: properties, behavior, and measurement of airborne particles, 2nd edition*. John Wiley & Sons, Inc.
- Lee, L. A., Pringle, K. J., Reddington, C. L., Mann, G. W., Stier, P, et al. (2013), The magnitude and causes of uncertainty in global model simulations of cloud condensation nuclei. *Atmospheric Chemistry and Physics*, *13*(17), 8879–8914. <https://doi.org/10.5194/acp-13-8879-2013>
- Lamaud, E., Brunet, Y., Labatut, A., Lopez, A., Fontan, J., and Druilhet, A. (1994), The Landes experiment: Biosphere atmosphere exchanges of ozone and aerosol particles above a pine forest, *J. Geophys. Res. Atmospheres*, *99*, 16511–16521, <https://doi.org/10.1029/94JD00668>, 1994.
- Liu, S., Lu, L., Mao, D., & Jia, L. (2007), Evaluating parameterizations of aerodynamic resistance to heat transfer using field measurements. *Hydrology and Earth System Sciences*, *11*(2), 769–783. <https://doi.org/10.5194/hess-11-769-2007>
- Matsuda, K., Fujimura, Y., Hayashi, K., Takahashi, A., & Nakaya, K. (2010), Deposition velocity of PM_{2.5} sulfate in the summer above a deciduous forest in central Japan. *Atmospheric Environment*, *44*(36), 4582–4587.

<https://doi.org/10.1016/j.atmosenv.2010.08.015>

Pleim, J., & Ran, L. (2011), Surface flux modeling for air quality applications. *Atmosphere*, 2(3), 271–302. <https://doi.org/10.3390/atmos2030271>

Pryor, S. C., Gallagher, M., Sievering, H., Larsen, S. E., Barthelmie, R. J., et al. (2008), A review of measurement and modelling results of particle atmosphere–surface exchange. *Tellus B: Chemical and Physical Meteorology*, 60(1), 42–75. <https://doi.org/10.1111/j.1600-0889.2007.00298.x>

Riemer, N., Ault, A. P., West, M., Craig, R. L., & Curtis, J. H. (2019), Aerosol mixing state: Measurements, modeling, and impacts. *Reviews of Geophysics*, 57(2), 187–249. <https://doi.org/10.1029/2018RG000615>

Saylor, R. D., Baker, B. D., Lee, P., Tong, D., Pan, L., & Hicks, B. B. (2019), The particle dry deposition component of total deposition from air quality models: right, wrong or uncertain? *Tellus B: Chemical and Physical Meteorology*, 71(1), 1550324. <https://doi.org/10.1080/16000889.2018.1550324>

Seinfeld, J. H., & Pandis, S. N. (2016), *Atmospheric chemistry and physics: from air pollution to climate change*. Third Edition. Wiley. ISBN: 978-1-118-94740-1

Shu, Q., Koo, B., Yarwood, G., & Henderson, B. H. (2017), Strong influence of deposition and vertical mixing on secondary organic aerosol concentrations in CMAQ and CAMx. *Atmospheric Environment*, 171, 317–329. <https://doi.org/10.1016/j.atmosenv.2017.10.035>

Shu, Q., Murphy, B., Pleim, J. E., Schwede, D., Henderson, B. H., Pye, H. O. T., Appel, K. W., Khan, T. R., & Perlinger, J. A. (2021), Particle dry deposition algorithms in CMAQ version 5.3: characterization of critical parameters and land use dependence using DepoBoxTool version 1.0. *Geoscientific Model Development Discussion*, [preprint], <https://doi.org/10.5194/gmd-2021-129>.

Slinn, W. G. N. (1982), Predictions for particle deposition to vegetative canopies. *Atmospheric Environment*, 16(7), 1785–1794. [https://doi.org/10.1016/0004-6981\(82\)90271-2](https://doi.org/10.1016/0004-6981(82)90271-2)

Sievering H. (1987), Small-particle dry deposition under high wind speed conditions: eddy flux measurements at the Boulder atmospheric observatory. *Atmospheric Environment*, 21(10), 2179–2185. [https://doi.org/10.1016/0004-6981\(87\)90350-7](https://doi.org/10.1016/0004-6981(87)90350-7)

Toyota, K., Dastoor, A. P., Ryzhkov, A. (2016), Parameterization of gaseous dry deposition in atmospheric chemistry models: Sensitivity to aerodynamic resistance formulations understatically stable condition. *Atmospheric Environment*, 147, 409–422. <https://doi.org/10.1016/j.atmosenv.2016.09.055>

Vong, R. J., Vickers, D., and Covert, D. S. (2004), Eddy correlation measurements of aerosol deposition to grass, *Tellus B*, 56, 105–117, <https://doi.org/10.1111/j.1600-889.2004.00098.x>, 2004.

- Wesely, M. L., Cook, D. R., & Hart, R. L. (1985), Measurements and parameterization of particulate sulfur dry deposition over grass. *Journal of Geophysical Research: Atmospheres*, 90(D1), 2131–2143. <https://doi.org/10.1029/JD090iD01p02131>
- Wesely, M. L., Cook, D., & Hart, R. L. (1983). Fluxes of gases and particles above a deciduous forest in wintertime. *Boundary-Layer Meteorology*, 27(3), 237–255. <https://doi:10.1007/BF00125000>
- Wigley, G., & Clark, J. A. (1974), Heat transfer coefficients for constant energy flux models of broad leaves. *Boundary-Layer Meteorology*, 7, 139–150. <https://doi:10.1007/BF00227909>
- Zhang, L., Gong, S., Padro, J., & Barrie, L. (2001), A size-segregated particle dry deposition scheme for an atmospheric aerosol module. *Atmospheric Environment*, 35(3), 549–560. [https://doi.org/10.1016/S1352-2310\(00\)00326-5](https://doi.org/10.1016/S1352-2310(00)00326-5)
- Zhang, J. & Shao, Y. (2014), A new parameterization of particle dry deposition over rough surfaces. *Atmospheric Chemistry and Physics*, 14, 12429–12440. <https://doi.org/10.5194/acp-14-12429-2014>